



Tribological performance of hybrid filtered arc-magnetron coatings

Part I: Coating deposition process and basic coating properties characterization

V. Gorokhovsky ^{a,*}, C. Bowman ^a, P. Gannon ^a, D. VanVorous ^a, A.A. Voevodin ^b, A. Rutkowski ^b,
C. Muratore ^c, R.J. Smith ^d, A. Kayani ^d, D. Gelles ^e, V. Shutthanandan ^e, B.G. Trusov ^f

^a Arcomac Surface Engineering, LLC., Bozeman, Montana, USA

^b Air Force Research Laboratory, Wright-Patterson AFB, Ohio, USA

^c UTC Inc./Air Force Research Laboratory, Wright-Patterson AFB, Ohio, USA

^d Montana State University, Bozeman, Montana, USA

^e Pacific Northwest National Laboratory, Richland, Washington, USA

^f Bauman Moscow State Technical University, Moscow, Russia

Received 15 June 2006; accepted in revised form 11 September 2006

Abstract

Aircraft propulsion applications require low-friction and wear resistant surfaces that operate under high contact loads in severe environments. Recent research on supertough and low friction nanocomposite coatings produced with hybrid plasma deposition processes was demonstrated to have a high potential for such demanding applications. However, industrially scalable hybrid plasma technologies are needed for their commercial realization. The Large area Filtered Arc Deposition (LAFAD) process provides atomically smooth coatings at high deposition rates over large surface areas. The LAFAD technology allows functionally graded, multilayer, super-lattice and nanocomposite architectures of multi-elemental coatings via electro-magnetic mixing of two plasma flows composed of different metal ion vapors. Further advancement can be realized through a combinatorial process using a hybrid filtered arc-magnetron deposition system. In the present study, multilayer and nanostructured TiCrCN/TiCr + TiBC composite cermet coatings were deposited by the hybrid filtered arc-magnetron process. Filtered plasma streams from arc evaporated Ti and Cr targets, and two unbalanced magnetron sputtered B₄C targets, were directed to the substrates in the presence of reactive gases. A multiphase nanocomposite coating architecture was designed to provide the optimal combination of corrosion and wear resistance of advanced steels (Pyrowear 675) used in aerospace bearing and gear applications. Coatings were characterized using SEM/EDS, XPS and RBS for morphology and chemistry, XRD and TEM for structural analyses, wafer curvature and nanoindentation for stress and mechanical properties, and Rockwell and scratch indentations for adhesion. Coating properties were evaluated for a variety of coating architectures. Thermodynamic modeling was used for estimation of phase composition of the top TiBC coating segment. Correlations between coating chemistry, structure and mechanical properties are discussed.

© 2006 Elsevier B.V. All rights reserved.

Keywords: Filtered arc; Magnetron; Coatings; Aerospace; Thermodynamics; Nanocomposite

1. Introduction

Aircraft propulsion elements, such as gears and bearings, operate under extreme conditions of high contact loads at high speed, and in aggressive environments. Corrosion attack in moist,

saline air is another critical factor that deteriorates surfaces of the tribological pairs if they are exposed to the environment. To provide both mechanical performance and corrosion resistance, advanced carburized stainless steels, e.g. Pyrowear 675 [64] and CSS-42L [65], were introduced for the use in aircraft gears and bearings. While these steels provide a balance between mechanical and corrosion properties, the friction contact areas are still subjected to both wear process and corrosion attack due to the tribochemical accelerated processes. In addition, broad

* Corresponding author. 3626 Fieldstone Dr., Bozeman, Montana, 59715, United States. Tel.: +1 406 522 7620; fax: +1 406 522 7617.

E-mail address: vigase@aol.com (V. Gorokhovsky).

temperature synthetic lubricants are often used on the tribological surfaces of military aircraft propulsion components. Some of these have a fluorinated chemistry [66], which provides a low viscosity at subzero temperatures, but can release aggressive fluorine agents at elevated temperatures via tribochemical reactions. For reliable operation of aircraft gears and bearings, advanced surface coating technologies are required to mitigate wear and corrosion processes in the contact areas.

Nanocomposite coatings with nanocrystalline/amorphous structures and functionally graded metal-ceramic interfaces with steel substrates have been designed to provide supertough characteristics and capability to withstand high contact loads of bearings and gears in aerospace systems [52–57]. Some of these coatings had contained nanocrystalline carbides embedded in hard amorphous diamond-like carbon (DLC) matrix, which helped to achieve a low friction and wear rates in ambient environments [58,59]. Such properties provide a safety margin of a non-catastrophic low friction and wear performance in an oil lubricant starvation as emergency back-up lubrication. Tribological carbon based coatings can be further improved with addition of carbide-forming non-metallic elements like Si, B, N in a multi-phase nanocomposite cermet structure [13–18,23–28]. Using boron as an alloying element for hydrogenated a-C:H films forms a structure with boron carbide crystals embedded in a-C:H matrix. Sputtered boron carbide coatings are now commercially produced on gears, molds, cutting and forming tools [27]. Complex boron containing carbides and carbonitrides are currently being explored for wear resistant applications [60]. Other carbon rich carbides are also successfully used for gears, bearings, and shafts [14–18,26,35].

Conventional thin film TiN and CrN cermet coatings have been used to prevent corrosion attack but have a limited success on tool steels because they are not thick enough to cover corrosion initiating surface defects sufficiently [1–4,42]. Even in the case of high chromium steel substrates like 440C or carburized Pyrowear 675, thin film coatings only protect against corrosion if a high substrate surface finish eliminates pitting initiation sites [1]. Incorporation of metallic interlayers into multilayer cermet coating, e.g. TiN/Ti or CrN/Cr, improves corrosion by the passivation capability of the incorporated metals [2–4,6]. Substrate pretreatment by plasma nitriding, carbonitriding or carburizing prior to coating deposition (duplex technologies) can also improve corrosion resistance [2–5,42]. Care should be taken to avoid substrate chromium depletion by forming nitrides and/or carbides, which could inhibit the passivation ability of the high chromium steels. Recently developed multiphase nanocomposite Cr-based nitride coatings such as (Ti,Cr)N, (Cr,Al)N have demonstrated improved corrosion resistance in comparison with single phase TiN or CrN cermets [2]. Further improvement in corrosion resistance can be achieved by adding non-metallic elements (C,B,Si) and by reducing the thickness of individual sublayers in the multilayer coatings to nanometer scale [2].

The production of advanced nanocomposite coatings of complex chemistry and nanostructure became possible with development of novel deposition processes, where plasma streams from several sources are combined, mixed, and directed toward the substrate with flexibility in a control of plasma che-

mistry, density, and energy [34,61]. Such flexibility is a critical requirement for both adhesion enhancing gradient structures and for the formation of advanced nanocomposite and nanolayer coating architectures. Supertough nanocomposite coatings developed in AFRL for high contact load applications were produced by a hybrid of magnetron sputtering-plasma laser deposition (MSPLD), where the high energy of the laser plasma was used to achieve a controlled crystallization [62]. Although promising, MSPLD is difficult to apply to large and complex substrate geometries, such as gears, due to the line of sight of the laser ablated plasma. Filtered vacuum arc is an alternative high energy plasma production source, which does not have this limitation, produces similar high quality carbon based coatings [63], and is very beneficial for the growth of well adhered and particle free metal and ceramic layers [32,33, 43,44].

A unique Large Area Filtered Arc Deposition (LAFAD) technology developed by Arcomac Surface Engineering LLC offers the opportunity for depositing advanced supertough nanocomposite coatings and corrosion resistant multilayer structures on very large and complex shaped surfaces of aircraft bearings and gears [32]. This process combines different types of plasma vapor sources working together in a common filtered arc plasma environment as achieved in the Filtered Arc Plasma Source Ion Deposition (FAPSID) surface engineering system [34]. The combination of large area filtered arc sources and unbalanced magnetron sputtering in the same chamber increases the metal ion flux conveyed by the plasma toward the substrate surface while keeping the flow of neutral atoms generated by magnetron sputtering fixed. This paper assesses the use of novel hybrid, large area filtered arc deposition-unbalanced magnetron sputtering (LAFAD-UBM) surface engineering technology, which was recently developed by Arcomac Surface Engineering LLC [34] for aircraft bearings and gears applications. Advanced coating architectures were designed, following the nanocomposite and functionally gradient concepts developed by AFRL for aerospace friction pairs [52–57]. These concept architectures were enhanced in this study by incorporation of corrosion mitigating multilayer nanocomposite coatings. Analyses and discussions of the coating mechanical properties, corrosion resistance and thermal-chemical synthetic lubricant compatibility on duplex treated coupons made of 440XH stainless steel and of Pyrowear 675 are provided in this paper.

2. Experimental

2.1. Hybrid FAD-UBM surface engineering technology

The FAPSID-700 surface engineering system featuring hybrid FAD-UBM technology is shown in Fig. 1. The FAPSID-700 consists of two dual large area filtered arc deposition (LAFAD) plasma sources, each having two opposite primary direct cathodic arc deposition (DCAD) sources with targets made of the same or different materials. The LAFAD uses a rectangular plasma-guide chamber with two pairs of rectangular deflecting coils installed on the opposite sides of the plasma-guide chamber, as shown in Fig. 1. In this work, two primary cathodic arc sources utilizing Cr and Ti targets were placed opposite to each other on the sidewalls

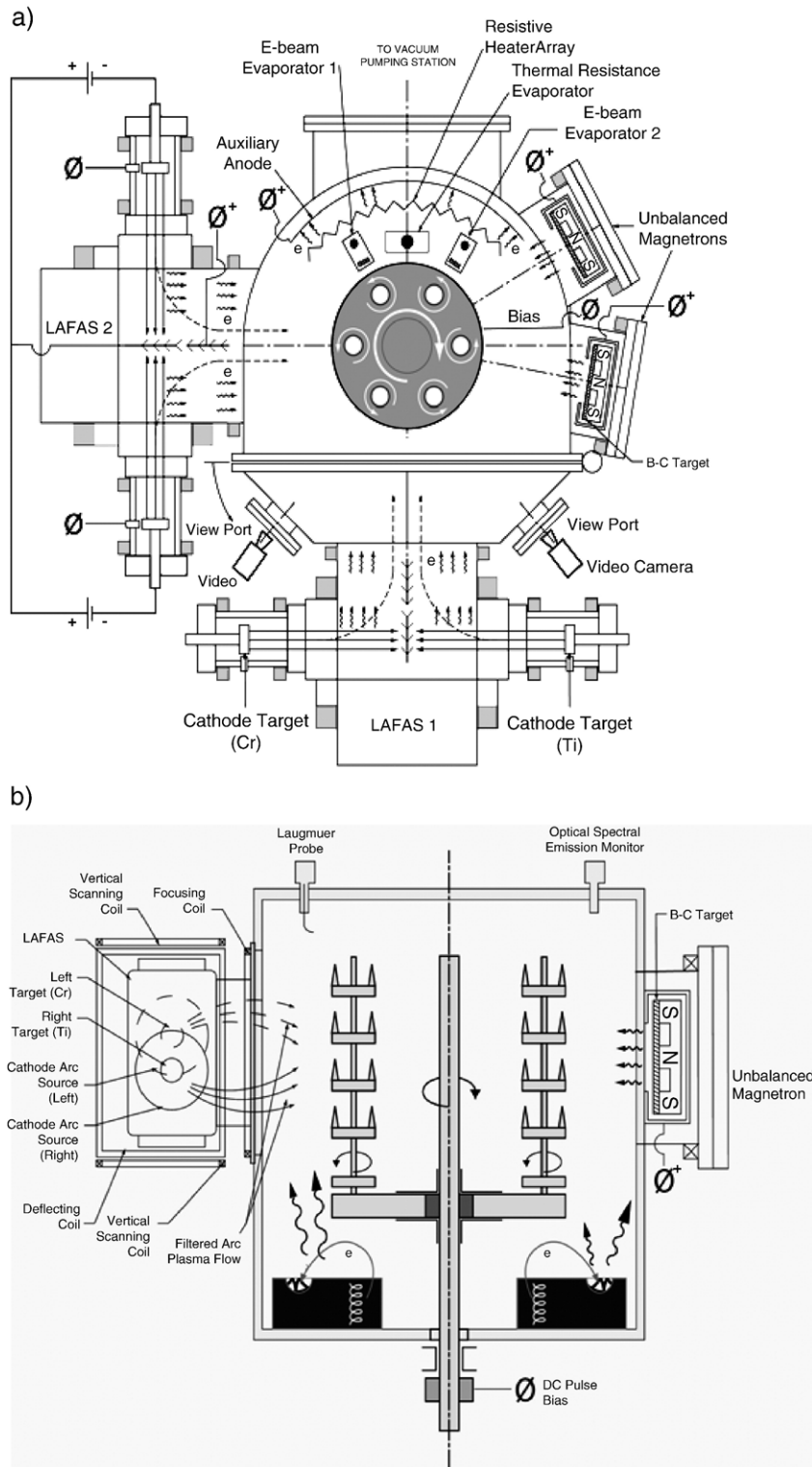


Fig. 1. Schematic illustration of ASE's FAPSID™ surface engineering system. This system utilizes Large Area Filtered Arc Sources (LAFAS) in a Universal Hybrid Layout with conventional PVD sources: (a) – top view, (b) – side view.

of the plasma-guide chamber, surrounded by rectangular deflecting coils, and separated by an anodic baffle plate. The LAFAD vapor plasma source uses a superimposed deflecting magnetic field to turn the metal ion flow 90° toward the deposition chamber and substrates [12,32]. The more massive droplets of material from the source follow straighter trajectories and are captured on

baffles, resulting in droplet-free coatings. A set of scanning magnetic coils allows the ion plasma jet to be swept in the vertical direction so as to cover theoretically unlimited large surface areas. At the same time, the arc column is well confined by a magnetic field in the horizontal direction, providing enhanced suppression of the turbulent plasma diffusion, leading to a significant increase

in the metal vapor ion yield. By manipulating the arc plasma jets using strategically placed scanning magnetic coils and auxiliary anodes, this design creates a “plasma-immersion” environment in the coating chamber. This technique allows the plasma flux from different cathodes in a multi-cathode chamber to be uniformly mixed and completely envelop complex parts. The use of auxiliary anodes in conjunction with the filtered arc sources permits extraction of a significant electron current from the arc source, which provides a highly conductive ionized gaseous plasma environment provides added versatility for such processes as ion cleaning, ionitriding, and ion implantation [32]. It was recently found that LAFAD plasma source can be combined with other PVD and low pressure CVD plasma sources in a universal hybrid multi-source chamber layout utilizing plasma flows generated by different PVD and CVD sources in filtered arc plasma immersion environment. This concept has been realized in FAPSID-700 surface engineering system design. In addition to two LAFAD plasma sources the FAPSID-700 system used in this work utilizes two unbalanced magnetrons with $102 \times 546 \times 3.2$ mm B_4C rectangular targets. This system is also equipped with two EB-PVD evaporators and resistive thermal evaporation (RTE) source all incorporated in one universal chamber layout. A universal layout provides the capability to deposit combinatorial coatings using hybrid LAFAD-UBM processes [34]. The substrates to be coated are installed into a carousel type multiple satellite substrate platform, which allows both single and double rotation of the substrates to be coated. A resistive heater array allows for heating of the substrates up to 450°C independently from plasma heating.

The following process parameters were typically used for the deposition of TiCrN/TiCr-TiCrCN bottom segment and transitional layer by LAFAD plasma source equipped with two (opposite) Ti and Cr targets. The arc currents were set on approximately 100 A for both Ti and Cr targets. The auxiliary arc discharge current was set on 150 A during argon ion cleaning stage and then reduced to 40 A during coating deposition stage. The substrate temperature did not exceed 350°C . An Advanced Energy Industry MDX-II power supply coupled with a Sparkle-V accessory unit was used as a bias power supply subsystem. The bias voltage was set at -250 V during ion cleaning stage followed by -1000 V during 2 min of metal ion

etching stage. The reverse time during ion cleaning/etching stages was set at $2\ \mu\text{s}$ at 48 kHz frequency. The bias voltage during coating deposition stage was set at -60 V DC. The TiCrN/TiCr multi-layer nanolaminated coating was deposited at 4×10^{-2} Pa gas pressure. Each bilayer in the TiCrN/TiCr multilayer architecture was deposited during 30 min with 25 min dedicated to TiCrN and 5 min to TiCr sublayers. The rotation speed of the substrate platform was set at 9 rpm, which corresponds to a 3–4 nm bilayer thickness in the {Ti based/Cr based} nanolaminated architecture, taking into account an approximately $1\ \mu\text{m/hr}$ deposition rate for both TiN and CrN coatings. The pure nitrogen was gradually changed to $\text{N}_2/40\%\text{CH}_4$ during a 40 min deposition of the intermediate TiCrCN layer. The preliminary set of samples was prepared with a TiCrC upper tribological segment deposited by LAFAD, on top of the transition TiCrCN layer using acetylene as a reactive gas at pressure of 5×10^{-2} Pa. Additional samples were produced with an upper layer consisting of TiBC nanocomposite cermet deposited by a hybrid filtered arc-unbalanced magnetron process. In this case both primary cathodic arc sources of LAFAD plasma source were equipped with Ti targets for generating titanium vapor plasma flow. The magnetron power density was set at approximately $5.5\ \text{W/cm}^2$. A small amount of reactive C_xH_y gas (acetylene or methane) was added to argon at a total gas pressure of 0.2 Pa. For deposition of multilayer TiBC/iBC (ML) coating architecture the deflecting magnetic field of the LAFAD plasma source was cycled off and on every 10 min. In contrast, the LAFAD deflecting magnetic field was activated continuously for deposition of the single layer TiBC (SL) coating architecture.

2.2. Duplex multilayer nanocomposite coating architecture

The coating architecture utilized in this work consists of two segments separated by an intermediate gradient zone as depicted in Fig. 2. The coating segment in contact with the substrate, the bond segment, is composed of a TiCrN based multiphase cermet. Periodic substrate exposure to Ti and Cr vapor plasma flows (Fig. 1) results in nanostructured ceramic and metallic layers in the $\text{MeC}_x\text{N}_{1-x}/\text{Me}$ multilayer nanolaminated architecture as shown in Fig. 3a. This provides substructure through a

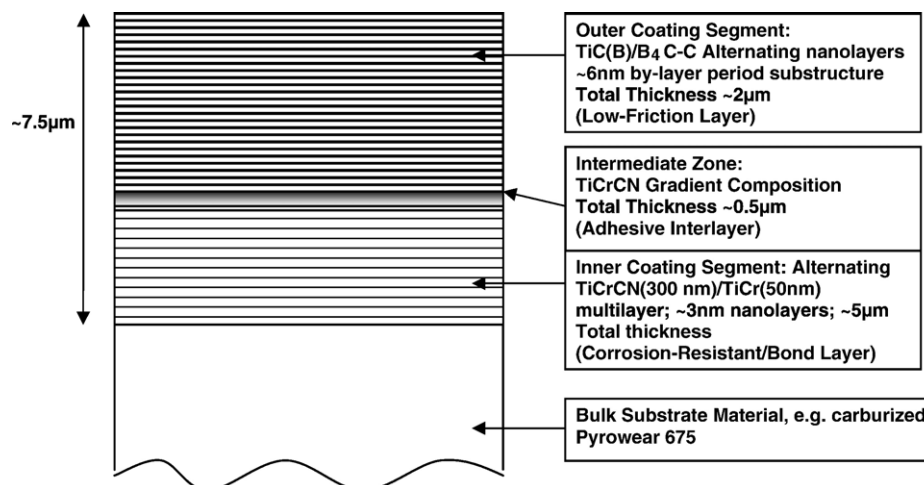


Fig. 2. Schematic illustration of the multilayer nanostructured functionally graded coating design used in this work.

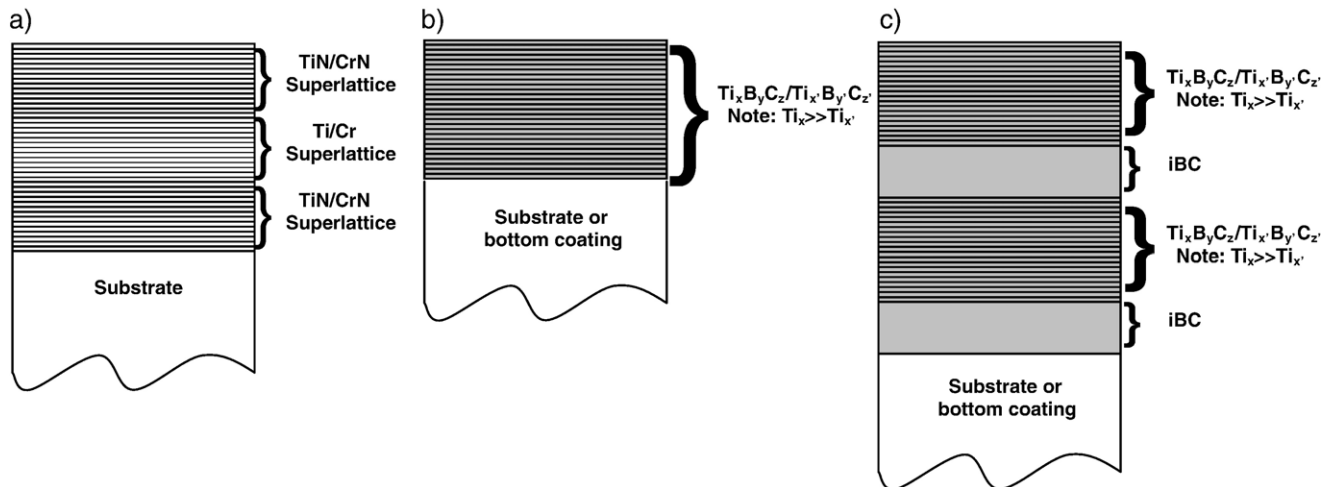


Fig. 3. Coating architecture of the bottom TiCrN/TiCr bond coating segment (a) and top TiBC coating segment (b, c) used in this work: the bottom segment has micrometric size multilayer with substructured nanolaminated periodic architecture; the top segment is deposited as either a nanocomposite single layer TiBC coating (b) or multilayer TiBC/iBC coating (c), where TiBC sublayers have the same nanocomposite structure as single layer TiBC coating shown in figure (b).

superlattice with a bilayer period at the nanometer scale. The bond layer substructure further improves toughness and stress management and is widely employed for corrosion resistant applications [5–7,10,25–30]. Simultaneously, the structure of the bond coating segment provides good adhesion and toughness, and can apply extensive compressive stresses to the substrate surface, made of chromium enriched carburized stainless steel such as Pyrowear 675. Using chromium-based cermet sublayers for enhancing coating adhesion is a well-known approach especially suitable for carbide, DLC, and Me-DLC coatings [25,28,31–34].

The upper segment, composed of TiBC nanocomposite cermet, was produced in two forms: as a single layer (SL) and as a TiBC/iBC multilayer (ML) structure utilizing TiBC layered with boron doped DLC layer as illustrated in Fig. 3b, c. This low friction coating is capable of operating in dry friction conditions as a solid lubricant material [2,27]. Adding boron carbide to the multi-phase tribological coating can improve corrosion resistance and thermal-chemical compatibility with lubricants at elevated temperatures. Sputtered boron carbide coatings are commercially produced and recommended for automotive gears operating under high frictional loads, molds, and cutting and forming tools [38–40]. In addition, boron carbide, as well as many other phases forming in a Ti–B–C system, is known to be chemically inert in extremely aggressive environments [29].

The intermediate zone, separating the inner and outer coating segments, consists of a graded composition providing smooth transition from the nitride-based inner coating segment, to the carbide based outer coating segment. This structure is tailored for optimal compatibility and stress management of the adjacent layers. This zone enhances the bond/adhesion of the outer (low friction) coating segment to the inner (corrosion resistant) coating segment.

Coupons, made of 440XH corrosion resistant martensitic stainless steel hardened to 62–64 HRC, were used during the preliminary experimental study. The 440XH coupons 6.4 mm dia × 3.2 mm thick with duplex treatment utilizing ionitriding

followed by a multilayer corrosion resistant tribological coating were prepared in a single plasma immersion vacuum cycle in the FAPSID-700 surface engineering system. When tests confirmed that the desired characteristics were obtained on the 440XH coupons, final trials were prepared on 25.4 mm dia × 6.4 mm thick disk coupons made of carburized Pyrowear 675.

2.3. Basic coating properties characterization techniques

Coating properties were characterized by variety of techniques. The following methods were used to determine the film's properties:

- (1) The coating thickness was measured by a spherical wear scar (Calotest™) technique.
- (2) The thickness of the ionitrided layer was determined by etching for 4 min in Nital followed by measurement using reflective optical microscopy.
- (3) Adhesion characteristics were determined using a Rockwell C 1450 N indentation test method specified by Diamler Benz. Its classification scheme, based on a HF1–HF6 scale, with a HF1 rating being the best is shown in Ref. [36].
- (4) A shank of a coated dental instrument was sheared by a standard ductility test device at different locations, and the coating delaminations around the sheared area were examined by optical microscopy. This test was also used for the measurement of ductility of the steel shanks.

Methods (1), (2) and (3) were applied to coated witness-coupons, since they require flat well-polished surfaces, while method (4) was used for evaluation of adhesion on coated round-shank dental instruments of different grades.

- (5) Scanning electron microscopy (SEM), high resolution transmission electron microscopy (HRTEM) and reflective

optical microscopy were used to examine morphology of films and instrument surfaces. The backscattering electron imaging (BEI) technique, which displays surface composition, was found to be beneficial for examining wear lands on coated instruments. In order to prepare specimens for HRTEM evaluation, it was decided that specimen preparation would be more efficient if the two samples were mounted with the coatings face-to-face so that both could be prepared simultaneously. Therefore, sections of each sample were cut about 2 mm wide and 10 mm long to contain the wear track in the center of the sample, the samples were glued face-to-face, the thickness of the composite was reduced to fit into a 3 mm (I.D.) tube, and 0.25 thick slices approximately 3 mm in diameter were cut. Slices were mechanically polished on one side using 1 m BN paste, glued to a molybdenum support washer and dimple ground on the other side using 1 μm BN paste leaving a sample thickness less than 15 μm . Gluing operations used a thermal setting epoxy that requires heating to $\sim 150^\circ\text{C}$ for a few minutes. Final thinning was by argon ion milling using a Precision Ion Polishing System (PIPS) from Gatan, Inc. operating at 5 KeV and a sputtering angle of 6° . Transmission Electron Microscopy (TEM) was performed on a JEOL 2010F with a field emission gun operating at 200 KeV. Scanning Electron Microscopy (SEM) was performed on a JEOL 840 operating at 40 KeV.

- (6) Surface profile was evaluated by atomic force microscopy (AFM).
- (7) XRD technique was used to identify phase composition in the coatings.

Further evaluation of adhesion and spallation resistance of the coatings was characterized by scratch testing with acoustic emission spectrometry. Adhesion and toughness of the coatings were evaluated with a CSEM scratch tester at AFRL, using a 0.2 mm diamond tip with a constant speed of 5 mm/min on the coating surface. The applied load was linearly increased up to 200 N with a rate of 50 N/min. The burst of acoustic emission was used to determine crack developments and gave a lower critical load for an estimation of the coating cohesion strength. The change of tangential friction force was used to determine penetration to the substrate and give an upper critical load for estimations of the coating adhesion strength [37]. Observations of the scratch paths were used to verify acoustic and friction force data. At least five scratches were performed for each coating and results were averaged to keep an experimental uncertainty within ± 5 N. Wear track profiles were investigated with Tencor P-10 contact profilometer, taking scan images of the track segments and calculating depth and width of the produced tracks.

The magnitude of residual coating stress was determined from the change in radius of curvature of Si wafers before and after deposition, using the Stoney equation [38] and assuming wafer elastic modulus of 180.5 GPa. A Tencor FLX-2320 thin film stress measurement system was used. For each coating, at least three measurements were performed and results were averaged.

The mechanical properties of coatings were investigated by nanoindentation measurements using an MTS Nanoindenter XP

system with a Berkovich diamond tip. Indentations were performed to a 500 nm displacement depth limit. The hardness and elastic modulus measurements were performed using a continuous stiffness monitoring mode (CSM) and applying a small amplitude tip oscillation. For all coatings, data was averaged over depth ranges when hardness and elastic modulus had minimum variations (exhibited plateaus) as a function of indentation depth to minimize both surface and substrate effects [39]. Ten indents were performed for each of the coatings and the results were averaged. Effective Young's modulus $E^* = E / (1 - \nu^2)$, where ν is Poisson's ratio of 0.2, and resistance to plastic deformation (H^3 / E^{*2}) was calculated from obtained hardness (H) and Young's modulus (E) data as in Ref. [60]. With each data set indentations into a fused SiO_2 standard were performed to ensure that the nanoindentation system remained calibrated.

Coating composition was analyzed by SEM/EDS and RBS techniques. E-beam energy of 9 kV was used for EDS analysis. In case of thin ($< 1 \mu\text{m}$) coatings the elements from the substrates were subtracted from EDS spectra. Ion beam analysis of the samples was performed using 3 MeV tandem accelerators at the Environmental Molecular Sciences Laboratory (EMSL) at Pacific Northwest National Laboratory (PNNL). Rutherford backscattering spectra (RBS), for the compositional analysis of the coatings, were recorded using a 2.5 MeV beam of He^+ ions with a 7° incident angle and 75° measured from the sample normal. Backscattered ions were collected using a silicon surface barrier detector at a scattering angle of 160° , with an exit angle of 40° from the sample normal. Hydrogen composition in the coatings was recorded using 2.5 MeV beam He^+ ions with an angle of incidence of 75° from the sample normal. Since hydrogen is lighter than He, it can only scatter in the forward direction; therefore, a silicon barrier detector was placed at a scattering angle of 30° with a 10 μm Al foil in front to stop the He particles from entering the detector. Because the Rutherford cross sections are more sensitive to heavier elements, B and C 2.5 MeV protons were used. At this proton energy, the scattering cross sections for B and C are non-Rutherford [40], producing enhanced scattering yields for these two elements. Finally, elemental compositions were determined by comparing SIMNRA computer simulations of the spectra obtained with the original data [41]. The spectrum was modeled in such a way that same composition fits all the spectra taken from the same sample with different beams. In addition, X-ray photoelectron spectroscopy (XPS, PHI Model 5600ci, Casa XPS Analytical Software) was performed to determine the concentrations and binding status of Ti, B and C within the TiBC coatings. XPS spectra were obtained after removing the surface layer of samples by sputtering with Ar^+ ions (3 keV, 15 μA) for 15 s and the spectra were calibrated for the value of the carbon peak C1 s at 284.5 eV.

3. Results

Post deposition AFM analysis demonstrated that surface roughness does not change substantially even after deposition of relatively thick (3–5 μm) TiCrCN/TiCr multilayer coatings. The LAFAD-UBM TiBC coatings with both ML and SL architectures

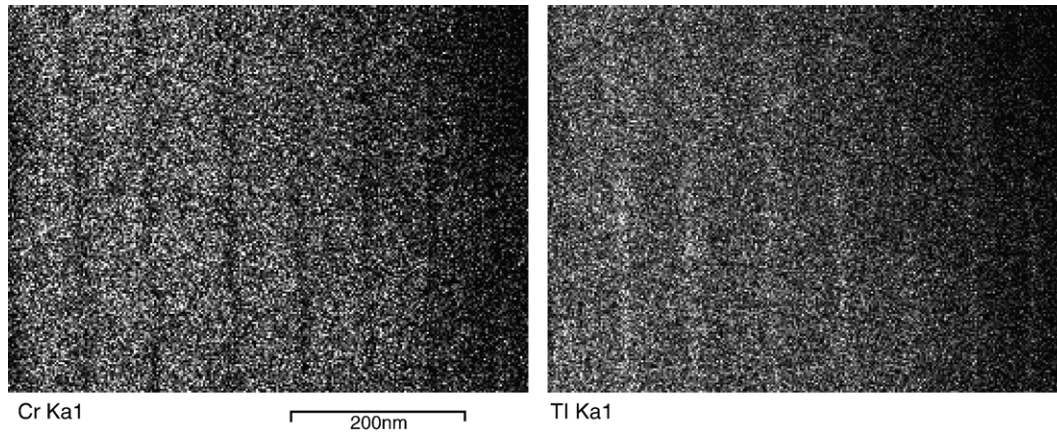


Fig. 4. Cr and Ti X-ray maps of a coating segment bottom bond coating segment showing systematic layers with reduced Cr levels and enhanced Ti levels. Note: the layers with low Cr and enhanced Ti signals are spaced at approximately 100 nm.

also demonstrated extremely smooth surface profiles. The 1 μm thick TiBC SL coating surface on Si wafer did not show any substantial increase in surface roughness relative to the initial roughness. Minor coating defects were observed as distant isolated pits. Auger spectra taken from these pits indicated the presence of a Ca as a likely cause of these surface defects which was associated with environmental dust particles.

The nanolaminated multilayer cermet coatings deposited by LAFAD technology has already been described elsewhere [33,43]. The micro-laminated structure consisting of TiCrN sublayers having thicknesses of approximately 100 nm can be seen in HRTEM mapping shown in Fig. 4. The TiCrN sublayers are separated by metallic interlayers having a thickness of approximately 10 nm. The dual-arc LAFAD process exposes the substrates in turn to Ti and Cr vapor plasma jets resulting in the

formation of a nanolaminated substructure in both TiCrN and TiCr sub-layers, illustrated by GD-OES spectra presented in Fig. 5 [33]. A HRTEM image of the nanolaminating substructure of the TiCrN sublayer in TiCr/TiCrN multilayer cermet coating used as the first (bottom) coating segment in this work is shown in Fig. 6. The bilayer period of TiCrN nanolayers results in a thickness of approximately 2.5 nm, which can be explained by rough estimation based on the deposition rate for TiCrN/TiCr coating of about 1 $\mu\text{m}/\text{hr}$ for substrates with single rotation arrangement paths in relation to the deposition sources [6,32,67,68]. At 9 rpm, substrates make 540 rotations per hour, which generates 540 biperiods each having thickness approximately 1.85 nm.

The results of the compositional analysis of the hybrid LAFAD-UBM TiBC coatings with different architectures were

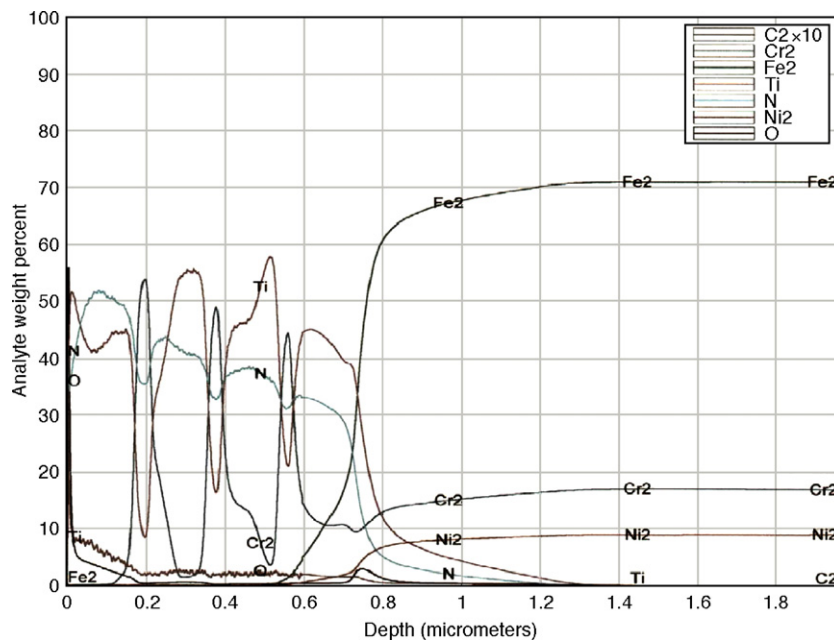


Fig. 5. GDOES spectra of TiCrN/TiCr nanolaminated cermet coating.

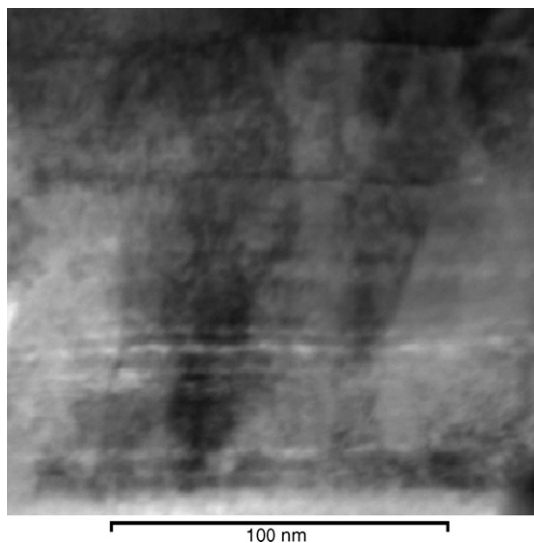


Fig. 6. HRTEM image of the TiCrN sublayer of a TiCr/TiCrN multilayer bond coating segment showing systematic nanolayer architecture with about 2 nm biperiod of TiN/CrN nanometric sublayers deposited by dual filtered arc LAFAD plasma source with primary cathodic arc sources equipped with Ti and Cr targets.

obtained by EDS/RBS techniques. Typical compositions of the TiCrCN transitional layer coating and TiBC upper tribological coating segment with ML and SL architectures are presented in Table 1. RBS and EDS techniques show similar results when coating thickness is greater than 1 μm . It can be seen that RBS provides better resolution of light elements. The carbon and boron concentration in TiBC (SL) and TiBC (ML) coatings are the same since both coatings have identical exposure to B_4C sputtering by UBM sources and carbon deposition from a HC/Ar auxiliary arc plasma environment. At the same time, Ti concentration is reduced in TiBC ML vs. SL coating due to interruptions of the titanium vapor plasma flow during deposition of multilayer TiBC coating architecture. The TiBC coating elemental composition defined by RBS vs. CH_4 flow rate for coatings deposited by different combinations of LAFAD/UBM plasma sources are shown in Fig. 7. Argon flow rate was constant at approximately 70 sccm, while CH_4 flow rate was set to 4 sccm, 8 sccm, and 16 sccm. Further increase in methane flow rate affects coating integrity: when CH_4 flow rate exceeds 18 sccm the carbon rich soot appears on the substrate fixtures and occasionally on substrates, especially when the substrates are processed with double rotation. Carbon

Table 1
Elemental composition of TiCrCN and TiBC coatings

Coating	Elemental Concentration at %					
	B	C	N	Ti	Cr	Ar
TiCrCN by EDS		28	27	31	14	
1 μm TiBC single layer EDS*/RBS	36/52	50/40	0	10/8	0	4/0
1 μm TiBC(5 min)/BC (15 min) multilayer EDS*/RBS	52/52	37/44	0	6/4	0	4/0

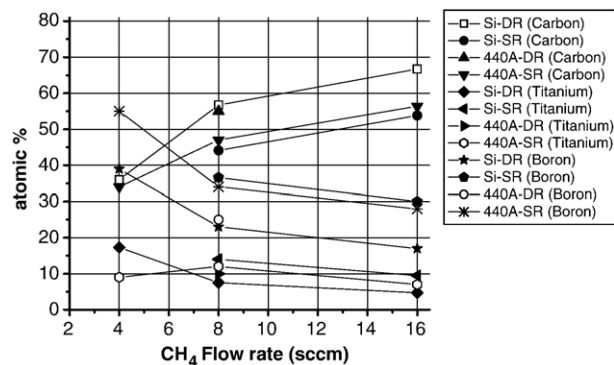


Fig. 7. TiBC coating elemental composition (at.% by RBS) vs. CH_4 flow rate.

concentration is increased for the coatings prepared with double rotation vs. single rotation, which can be attributed to higher level of exposure of double rotating surfaces to hydrocarbon plasma environment. The carbon concentration increases, while concentrations of Ti and B decrease when methane flow rate increases. The XPS spectra taken from two samples with TiBC coatings deposited by FAD/UBM process with 8 sccm methane flow rate show a strong evidence of large free carbon concentration in the coating in addition to boron carbide phase as illustrated in Fig. 8.

Nanoindentation (Berkovich) was measured for selected P675 coupons with different TiCrCN+TiBC coatings. An example of the nanoindentation data obtained with a CSM mode is shown in Fig. 9. From this figure, data was leveled at indentation depths between 100 and 300 nm for both hardness (Fig. 9a) and elastic modulus (Fig. 9b). This analysis helped to select indentation depth regions for data averaging when both surface and substrate effects on the indentation response were minimized. The average H and E values were obtained in a similar way for all coatings and results are summarized in Table 2. It can be seen that the hardness of the TiCrCN bottom coating segment is about 20 GPa, which is slightly less than the hardness of TiCN/Ti multilayer coatings deposited by LAFAD technology (~ 25 GPa [33,43]). These results are in agreement with the data obtained by load-displacement method in [44] for the same

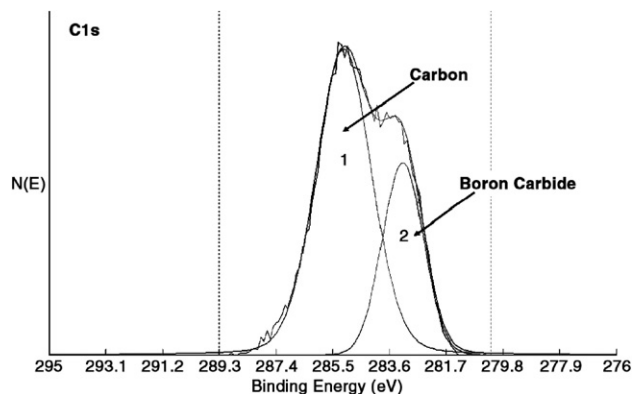


Fig. 8. X-Ray photoelectron spectrum showing carbon peak from typical TiBC coating. Note: $\sim 70\%$ of carbon is bound to itself (amorphous C matrix), whereas $\sim 30\%$ is B_4C (embedded nanocrystallites). Courtesy of Jim Anderson.

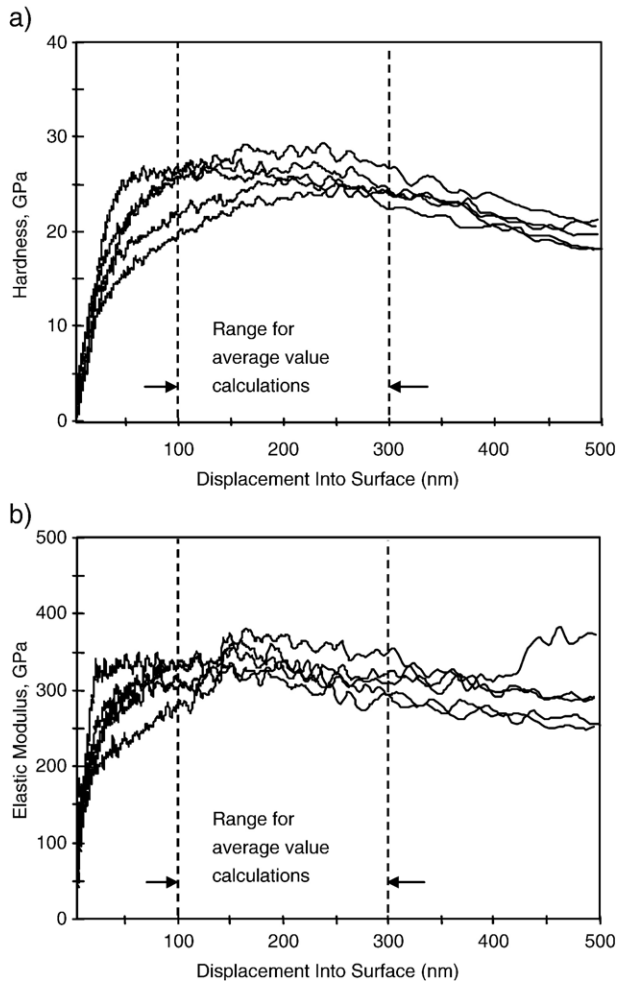


Fig. 9. Examples of nanoindentation data for a) hardness and b) elastic modulus obtained with a continuous stiffness monitoring mode for a TiBC (SL) coating on Pyrowear 675 substrate. Average values of hardness and elastic modulus were calculated over indicated range where their dependence on the indentation depth was minimized. Individual curves represent repeated indentations in different sample locations (only five are shown for clarity).

type of coatings. The nanohardness for two-segmented TiCrCN + TiBC coating is higher, ranging from 23–25 GPa. The nanohardness results for relatively thin (0.3–0.5 μm) coatings on Si wafer substrates are influenced by substrate deformation

(indentation depth 500 nm), which explains the observed lower absolute nanohardness values for these coatings in comparison with 25 GPa for relatively thicker (~1.5 μm) TiBC coatings deposited on Pyrowear 675. The substrate effect is further emphasized by the consistent trend towards lower nanohardness in double rotation samples, which have ~60% coating thickness versus single rotation samples. Nevertheless, nanohardness results from each coated sample can be correlated to the vapor process combinations and hydrocarbon flow rates. Results show that control of hydrocarbon flow rates during coating deposition has a marked effect on the resulting coating nanohardness with the highest nanohardness of 25 GPa and 18.4 GPa on Pyrowear 675 and Si respectively for TiBC at 8 sccm CH₄, followed by slightly lower nanohardness of 17.7 GPa on Si results for a B₄C coating deposited without hydrocarbon gas addition. The calculated value of H^3/E^{*2} which has been shown to be related to resistance to plastic deformation and coating toughness [83,84] was found to be in the range of 0.060 GPa–0.167 GPa for the deposited coatings, and also dependent on hydrocarbon flow rate, with the highest value of 0.167 GPa demonstrated for the TiBC architecture at 8 sccm CH₄.

During initial development of TiCrN/TiCrCN/TiCrC coatings, adhesion by Rockwell C (1450 N) indentation testing revealed that the bottom TiCrCN coating deposited by LAFAD process maintained high adhesion in all cases, while top segment thin TiCrC carbide layers showed frequent delamination (HF5HF6). Adhesion testing of the TiCrCN+TiBC coatings by Rockwell C (1450 N) indentation, revealed much higher adhesion of the top TiBC layer (HF1HF3) as compared to TiCrC top layer, and as a result TiBC coatings were selected for further development with (SL) vs. (ML) architectures as the primary variable. It was found that TiBC (SL) in most cases demonstrated better adhesion than TiBC (ML). The TiBC/BC multilayer structure was found to exhibit interlayer delamination failure at multilayer interfaces. The worst adhesion was found on samples having a TiBC/BC multilayer ~1.5 μm segment followed by a TiBC ~1.5 μm segment (HF6 delamination to 2× radius of the indent). The combined adhesion results demonstrate that the maximum thickness of the top TiBC layer is limited to approximately 11.5 μm, due to high stresses in this nanocomposite coating. Conversely, the thickness of the bottom TiCrCN segment does not appear to be a

Table 2
Hardness, elastic modulus and resistance to plastic deformation parameter (H^3/E^{*2}) for coatings deposited by hybrid LAFAD/UBM process vs. process parameters

Coating	TiCrN (LAFAD source only)	TiBC (SL)	TiBC (ML)	TiCrC	TiBC	TiBC	TiBC	TiBC	BC	TiBC
(Gas, flowrate)		(CH ₄ , 8 sccm)	(CH ₄ , 8 sccm)	(CH ₄ , 8 sccm)	(CH ₄ , 4 sccm)	(CH ₄ , 8 sccm)	(CH ₄ , 12 sccm)	(CH ₄ , 0 sccm)	(CH ₄ , 0 sccm)	(C ₂ H ₂ , 4 sccm)
Rotation	SR	SR	SR	SR DR	SR DR	SR DR	SR DR	SR DR	SR DR	SR DR
Substrate	Pyrowear 675	Pyrowear 675	Pyrowear 675	Si Si	Si Si	Si Si	Si Si	Si Si	Si Si	Si Si
Residual stress [GPa]	-0.17	<-1	<-1	<-1 <-1	<-1 <-1	<-1 <-1	<-1 <-1	<-1 <-1	<-1 <-1	<-1 <-1
H [GPa]	21	25	24	14.5 12.7	16.0 14.6	18.4 16.4	12.7 11.2	17.7 14.1	15.4 11.5	
E [GPa]		325	285	179 169	197 174	181 178	176 143	185 183	179 139	
H^3/E^{*2} [GPa]		0.14	0.16	0.084 0.063	0.093 0.090	0.167 0.122	0.058 0.060	0.142 0.074	0.100 0.069	

Table 3
Summary of scratch test results for selected TiCrN+TiBC coatings on carburized pyrowear 675

	Sample description		
	TiCrN 1.3 μm^*	TiCrN 1.3 μm	TiCrN 1.3 μm
	TiBC (SL) 1 μm^{**}	TiBC (SL) 1 μm	TiBC (SL) 1 μm
Lower critical load (N)	47+/-11	30+/-3	23+/-2
Upper critical load (N)	124+/-3	122+/-8	113+/-4

*Bottom segment, **top segment.

significant variable in terms of the overall two-segment coating adhesion. Acoustic emission scratch test results supported the Rockwell indentation results by exhibiting large variations between upper and lower critical load values, indicating initial top segment failure. Measured lower critical load values correlated to initial fracture and delamination of the top segment architecture from the bottom segment. Complete coating failure and removal from the scratch track was measured as an upper critical load value. Excellent adhesion was indicated by upper critical load values that were consistently measured between 100 N to 120 N. The best lower critical load values were demonstrated by TiBC(SL) top segment architectures. Independence from top segment architecture in upper critical load measurement was observed, which indicated that measured upper critical values represented bottom segment adhesion. A summary of the scratch test results obtained by AFRL is shown in Table 3.

4. Discussion

Carbon rich carbides are well known for their ability to combine high wear resistance with low friction at high contact loads, which make them attractive for machine parts applications like gears, bearings, shafts, etc. [14–18,26,35]. In nanocomposite coatings deposited by FAD/UBM process, the hard amorphous carbon matrix, similar to DLC coatings consisting of a highly cross-linked network of carbon atoms, formed under high fluxes of ionized atoms conveyed by the plasma to substrates [9–25]. Using co-deposition of MeC and carbon from two or more sputtering or evaporating sources in addition to dissociated hydro-carbon reactive gaseous plasma can achieve the highest functional properties, while processing at relatively low temperatures, and without significant hydrogen concentration in the process gas environment [16,17,35]. Boron forms hard and corrosion resistant compounds with titanium, chromium and carbon, which are widely used for surface engineering and in the cermet industry [11–18,27,29]. Incorporating hard phases of transitional metal carbides and borides within the amorphous carbon matrix controls stresses and increases wear resistance and critical load, while retaining low friction [8,10,11,21,23]. It allows the improvement in coating toughness, while retaining a relatively high hardness comparable to conventional hard cermet coatings.

The extreme conditions near the substrate surface created by metal-gaseous ion bombardment (multi-charged metal ion

energies ranging from 40 to 200 eV) result in high-energy dissipation at localized collision areas on the substrate surface [45,75,78]. During a very short time period, associated with energy relaxation of ions bombarding the growing film, the equivalent temperature in these areas can substantially exceed the bulk substrate temperature. Effectively, a dramatic increase in ion-substrate interactions and chemical reactivity is realized. In this environment, new compounds form at rates which surpass those predicted by the associated Arrhenius rate laws at the bulk substrate temperature [10–14,45,75,78,79]. In the FAD/UBM TiBC coating deposition process, individual sources of Ti, B, C are separately controlled. In addition, the selected positioning of these sources in the FAPSID chamber layout permits substrate exposure to different deposition vapor flows (e.g. Ti, B, C) during the coating process (Fig. 1). In case of single rotating substrates, Ti plasma vapor is conveyed directly towards the substrates from LAFAD plasma source and indirectly by resputtering of Ti from the UBM target surfaces. B and C species are co-sputtered from the UBM sources. In addition, carbon and carbon containing CH_x radical species are generated as dissociation products from methane-containing gaseous plasma atmosphere. The dual rotating substrates experience increased exposure to gaseous carbon-containing plasma compared with single rotating substrates, which results in lower concentrations of Ti and/or B within these films (Fig. 7). During exposure to methane-precursor gaseous plasma only, the conditions are favorable to the formation of diamond-like carbon [75,79]. With the intense ion-bombardment inherent in the FAPSID system, the sp^3/sp^2 ratio within the resultant a-C coating increases. When Ti and/or B sources are employed in conjunction with the a-C plasma deposition environment, multiple Ti–B–C containing crystalline phases form depending upon the substrate position within the FAPSID system. The XRD patterns presented in Fig. 10 illustrate this occurrence. Peaks identified in these patterns demonstrate the coexistence of strongly crystallized TiB_2 with weakly crystallized $\text{Ti}_x\text{B}_y\text{C}_z$ solid solution phases in the FAD/UBM coatings. The sharp TiB_2 peak indicates strong crystallinity compared with the relatively broad peaks of the $\text{Ti}_x\text{B}_y\text{C}_z$ solid solution phases, indicating the nanocrystalline nature of the solid solution constituents. The exact composition of this ternary solid solution resembles the $(\text{B}_{12})_4\text{Ti}_{1.86}\text{C}_2$ ternary phase having a tetragonal boron structure described in [80]. The near-surface conditions of intense ion bombardment in the FAD/UBM process may also permit formation of other refractory crystalline phases, e.g. TiC, TiB, B_4C and their nonstoichiometric forms; however, due to the extremely small crystallite sizes, these phases will remain undetected via XRD.

Thermodynamic modeling was employed to assess the favored phase compositions of FAD/UBM TiBC coatings. Thermodynamic equilibrium calculations were used to simulate favored mixtures of individual phases and solid solutions at elevated temperatures in the Ti–B–C based coatings. According to the second law of thermodynamics, for the calculation of phase equilibrium in isolated multicomponent system, containing gaseous phase components, immiscible condense phase components and solid solutions, it is necessary to maximize the

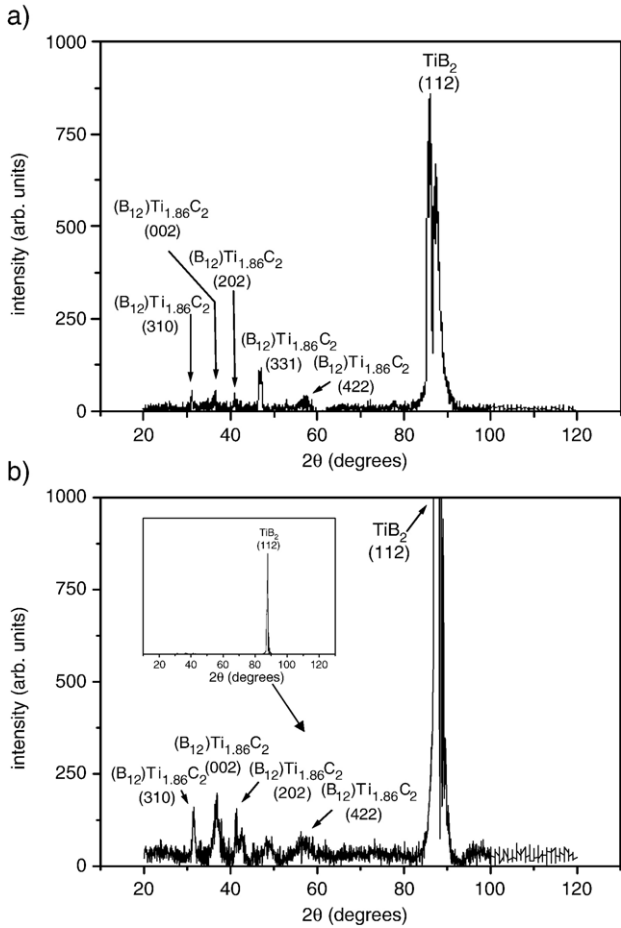


Fig. 10. XRD spectra taken from two samples with TiBC nanocomposite cermet coating deposited by two different FAD/UBM processes with different methane flowrates. (a) – Sample No.41 (8 sccm CH₄): Ti(6 at.%)C(53 at.%)B(26 at.); (b) – sample No.49 (0 sccm CH₄): Ti(15 at.%)C(15 at.%)B(25 at.%). Note: PDF card numbers used to identify peaks: TiB₂: 35-0741; (B₁₂)₄Ti_{1.86}C₂: 73-0658.

total entropy of the system. This can be presented in the following form [46]:

$$S = \sum_{i=1}^k S_i^{(p_i)} \cdot n_i + \sum_{r=1}^R S_r \cdot n_r + \sum_{x=1}^X \sum_{q=1}^{Q_x} S_{xq} n_{xq}$$

$$= \sum_{i=1}^k \left(S_i^0 - R_0 \ln \frac{R_0 T n_i}{v} \right) \cdot n_i + \sum_{r=1}^R S_r^0 \cdot n_r$$

$$+ \sum_{x=1}^X \sum_{q=1}^{Q_x} \left(S_{xq}^0 - R \ln (n_{xq} / n_x) \right) \cdot n_{xq}$$

where k is the number of gas phase components; R is the number of a single immiscible condense phase components; X is the number of solid solutions; Q_x is the number of components in a solid solution x ; $S_i^{(p_i)}$ is the entropy of gas phase component i at the partial pressure $p_i = R_0 T n_i / v$, which it will have in the equilibrium state; v is specific volume of the entire system; S_i^0 is the standard entropy of gas phase component i at the temperature T and pressure of 1 atm; S_r^0 is standard entropy of a single condense phase component r , which is a function of temperature only; S_{xq}^0 is standard entropy of the component q of the solid solution x .

To determine the parameters in the equilibrium state it is necessary to find the values of all variables, including mole fractions of all components when the entire entropy of the system S reaches its maximum with certain additional conditions applied on the system. These additional conditions include: the conservation of the total internal energy of the system, as the system is isolated; the conservation of the total mass of all components of the system; and electroneutrality condition:

$$-U + \sum_{i=1}^k U_i \cdot n_i + \sum_{r=1}^R U_r \cdot n_r + \sum_{x=1}^X \sum_{q=1}^{Q_x} U_{xq} \cdot n_{xq} = 0;$$

$$b_j = \sum_{i=1}^{k+R+X} a_{ji} n_i, \quad (j = 1, 2, \dots, m); \quad \sum_{i=1}^k a_{ei} n_i = 0,$$

where U is the total internal energy of the system, U_i, U_r, U_{xr} – are internal energy the gas phase components, single immiscible components of condense phase and components of solid solutions respectively; b_j – mole fraction of the element j in the system; a_{ji}, a_{ei} – stoichiometric coefficients. In case of a regular solution model, the partial enthalpy of mixing has to be added to the total internal energy of solid solutions in addition to the internal energies of components. In the ideal solution model used in this work the enthalpy of mixing is assumed to be zero. In addition, the normalization conditions have to be satisfied for each of the solid solutions:

$$\sum_{q=1}^{Q_x} \frac{n_{qx}}{n_x} - 1 = 0, \quad n_x \geq 0, \quad (x = 1, 2, \dots, X)$$

To perform these calculations, the thermodynamic equilibrium code, TERRA was employed. TERRA is a recently developed version of the ASTRA code, which was used extensively for thermodynamic modeling in Eastern Europe during the 1980s–1990s [46]. Its database includes most of the refractory compounds properties compatible with SGTE and JANAF-NIST databases [47,48,69]. Various models of the Ti–B–C

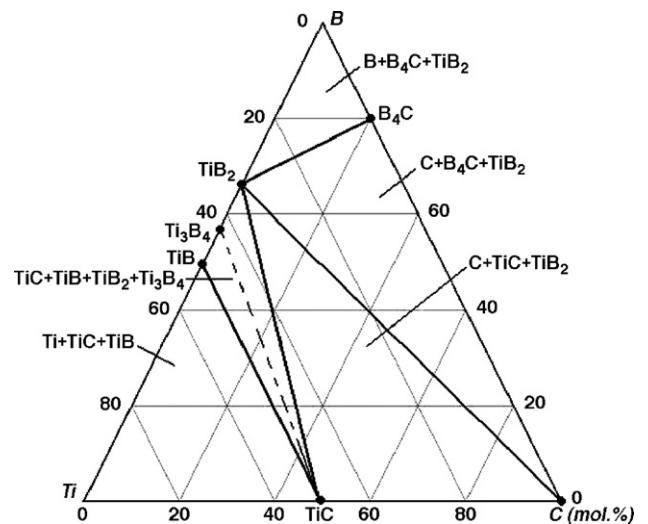


Fig. 11. TiBC ternary phase diagram at $T=700$ K, $p=0.1$ Pa.

system were prepared within the temperature range of 300 °C to 1100 °C at a constant pressure of $P=10^{-3}$ Torr. These conditions closely resemble those of the hybrid FAD/UBM TiBC coating deposition process, which provides intense ion bombardment during coating material vapor condensation. A calculated ternary phase diagram of TiBC system at 700 K and 0.1 Pa (typical FAD/UBM TiBC deposition conditions) is shown in Fig. 11. This calculation takes into account the individual stoichiometric

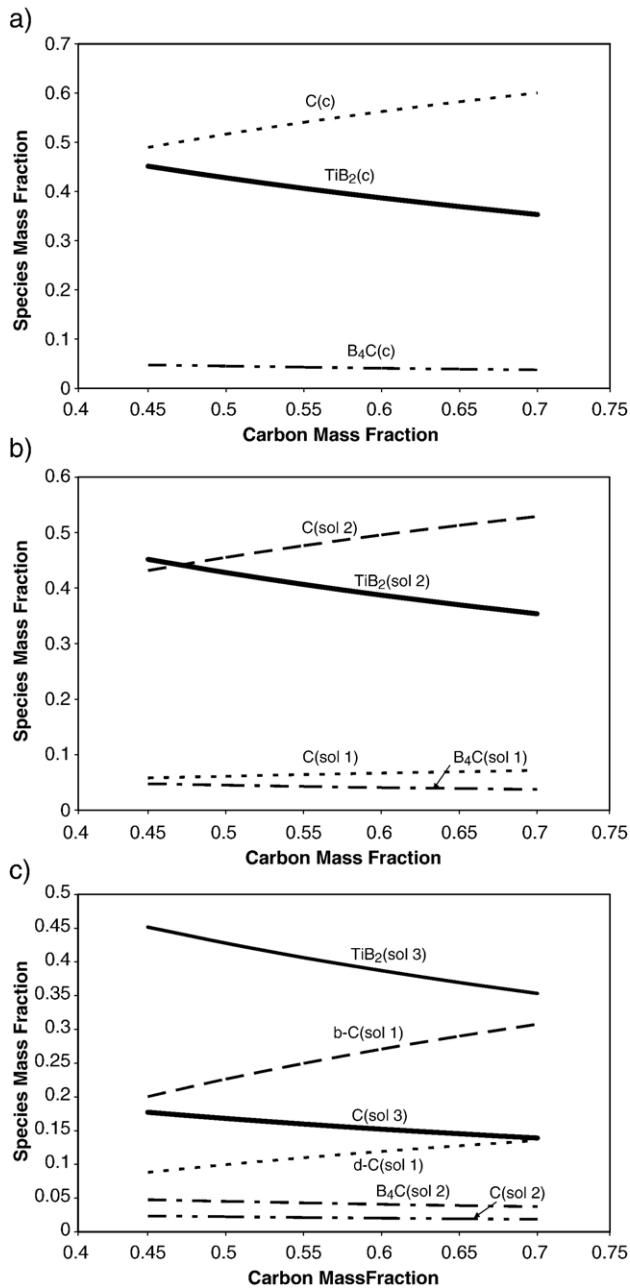


Fig. 12. Thermodynamic modeling results (see detailed modeling parameters in Table 4): a – high boron composition, no solid solutions, with bC (β -Graphite) as the free carbon phase; b – high boron composition, solid solutions without free carbon phase; c – high boron composition, solid solutions with bC+dC solid solution as the free carbon phase; d – high boron composition, solid solutions with bC+aC solid solution as the free carbon phase; e – low boron composition, solid solutions with bC+aC solid solution as the free carbon phase.

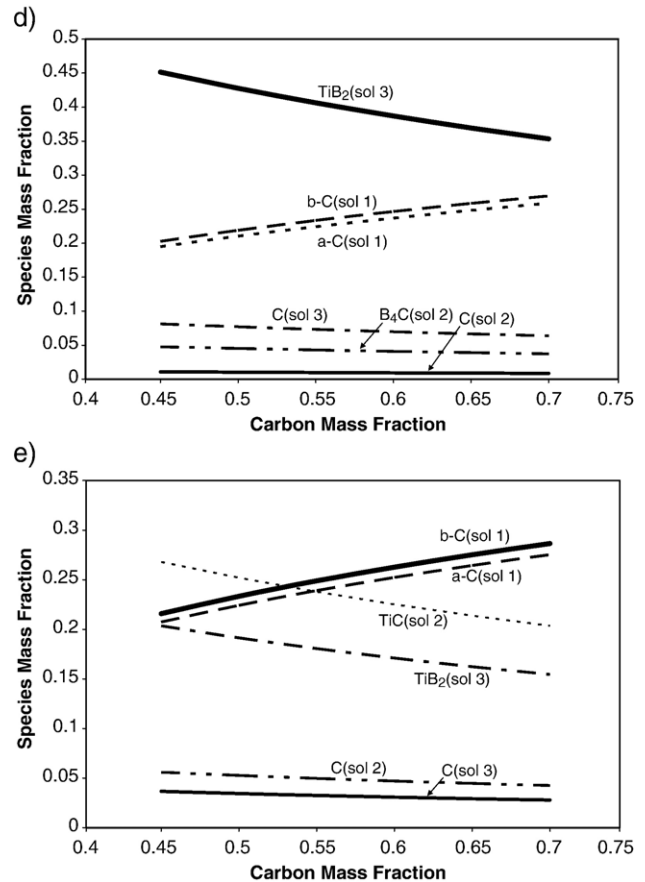


Fig. 12 (continued).

compound phases only, which can be considered as a zero-order approximation, providing that it does not take into account solid solutions in the TiBC system. The Ti_3B_4 phase was not included in this calculation. The data associated with this phase is shown in Fig. 11 as it appears in the modeling diagram, calculated by Gusav et al. [49]. The results show that titanium diboride coexists either with TiC or with B_4C . Free carbon (β -Graphite phase) co-exists with both $TiB_2 + B_4C$ and $TiB_2 + B_4C + C$ compositions. No ternary TiBC compounds are found in this system. This phase composition exists in wide range of pressures (1 MPa–0.1 Pa) and temperatures (up to 1800 K). These results are in a good agreement with more precise calculations and experimental data with exception of very narrow area boarding between $\{TiB_2 + TiC + C\}$ and $\{TiB_2 + B_4C + C\}$ areas where TiB_2 coexists with TiC and B_4C , which took into account non-stoichiometric compounds and solid solutions as well as phase diagrams based on experimental data [49–51,69,72–74,86]. Similar results were obtained recently for B–C–N coatings deposited by reactive magnetron sputtering [71]. In this case, the ternary compounds were found to be a small impurity in amorphous films composed of boron, carbon and nitrogen and contained B=C, B=N, C=N, C=C covalent bonding.

Further calculations were performed with different potential solid solution compositions presented in the TiBC elemental system. These calculations were based on ideal solution model as a first-order approximation. This included modeling of

diamond-like carbon phases, whose formation is induced by high compressive stresses and thermal spikes from co-incidental ion bombardment of the growing film. These created conditions for the formation of high pressure sp^3 coordinated (diamond like) phases such as tetrahedral amorphous carbon in addition to sp^2 coordinated (graphite like) carbon [75,78,85]. Two approaches were used for modeling such amorphous carbon mix in the TiBC system. In the first approach, amorphous carbon was modeled as an ideal solid solution including β -graphite (bC) and diamond (dC). In the second approach, free carbon was modeled as an ideal solid solution including β -graphite (bC), having enthalpy of formation $H_f(\text{bC})=0$ as the basic elemental phase, and a hypothetical amorphous carbon (aC) carbon phase, having enthalpy of formation $H_f(\text{aC})$ ranging from 200 to 1000 J/mol K while other thermodynamic parameters (entropy, specific heat capacity) were taken equal to that of graphite. Thermodynamic properties of diamond phase were taken from Refs. [70,81]. Examples of typical results from these calculations presenting phase composition vs. carbon content are shown in Fig. 12a–e. The elemental compositions chosen for this modeling resemble the experimental results from the hybrid FAD/UBM TiBC coating deposition processes, as shown in Fig. 7. Two sets of elemental compositions were considered in these calculations: one with higher boron content; and another one with lower boron content. These sets describe two experimental situations in the FAD/UBM process: when the substrates to be coated are positioned near titanium LAFAD vapor plasma source (lower boron concentration in the coating); and, when the substrates are positioned near UBM sputtering source with B_4C targets (higher boron concentration in the coating). The set of compounds and solid solutions used in these calculations are presented in Table 4. It includes solid solutions of carbon in carbides and TiB_2 , binary solutions of carbides and borides, solution of boron in B_4C , and solution of titanium in TiC and in TiB_2 . TiB_2/B and TiC/B solutions were not included since boron has very low solubility in TiB_2 and TiC at temperatures below 2000 K [68,72–74,86].

The compositions in Fig. 12a assumed that β -Graphite (bC) is the only free carbon phase and there are no solid solutions of carbon in carbide phases. It can be seen that in all cases TiB_2 and B_4C phase concentrations decreased when the free carbon concentration increased. The concentration of TiB_2 was much greater than B_4C . The TiC phase did not co-exist with TiB_2 and B_4C when the elemental composition with increased boron concentration is considered. This result is in good agreement with the ternary phase diagram (Fig. 10). The results of calculations shown in Fig. 12b used the same elemental composition as in Fig. 12a, but 16 binary ideal solid solutions were taken into account (see Table 4) and free carbon was allowed to form solid solutions with other phases. From the calculation results, only two solid solutions could co-exist: TiB_2/C and B_4C/C . No independent stoichiometric phases are thermodynamically favorable along with corresponding solid solutions. In this case all the carbon formed solid solutions with Ti and B and carbon solubility increased with carbon content. In this model, the carbon solubility reaches levels which are much above the known solubility of carbon in B_4C

Table 4

Phase composition considered in thermodynamic modeling of the TiBC coatings (Fig. 12)

	Fig. 12a	Fig. 12b	Fig. 12c	Fig. 12d	Fig. 12e
Ti/B (mol/kg)	2.8/1.6	2.8/1.6	2.8/1.6	2.8/1.6	2.8/0.5
<i>Stoichiometric phases</i>					
B_4C	X				
TiB_2	X				
TiC	X				
bC (β -Graphite)	X				
<i>Ideal binary solid state solutions</i>					
bC+aC				X	X
bC+dC			X		
bC+ B_4C		X	X	X	X
bC+TiC		X	X	X	X
bC+ TiB_2		X	X	X	X
TiB_2 + TiB_2		X	X	X	X
TiC+ TiB_2		X	X	X	X
B_4C + TiB_2		X	X	X	X
TiC+ B_4C		X	X	X	X
Ti+ TiB_2		X	X	X	X
Ti+TiC		X	X	X	X
Ti+ B_4C		X	X	X	X
B+ B_4C		X	X	X	X
B+TiC		X	X	X	X
B+ TiB_2		X	X	X	X
TiB_2 +TiC		X	X	X	X
TiB_2 + B_4C		X	X	X	X

Note: bC- β -Graphite ($H_f=0$); aC-hypothetical amorphous carbon phase with increased C=C bonding energy ($H_f=200\div 1000$ J/mol K); dC-diamond ($H_f=1895$ J/mol K [81], Cp is taken from Ref. [70]).

and TiB_2 from prior phase diagram calculations and experimental data [50,71].

As a further model development, a substantial increase of sp^3 bonds in the amorphous carbon matrix was taken into account and the free carbon phase in the coating was modeled as an ideal solution of β -graphite (bC) and diamond which has the highest enthalpy of formation of all carbon phases. The calculation results shown in Fig. 12c used the same elemental composition (higher boron) as in Fig. 12b, including the 16 solid solutions as considered in Table 4 in addition to a graphite–diamond solution. These results are similar to the results presented in Fig. 12a with a clear increasing trend of the free carbon phase concentration, and a decrease of TiB_2/C and B_4C/C solid solution concentrations with increase of carbon content. However, in Fig. 12c, the solubility of carbon does not exceed 20%, which agrees with data on carbon solubility in these compounds. The concentration of sp^3 coordinated carbon in the amorphous carbon matrix is below 30%. For more realistic simulation of the amorphous carbon phase formed by vapor condensation with ion bombardment, the following considerations were taken into account. The amorphous carbon coatings formed by sputtering of carbon containing targets and dissociation of C–H gaseous species under condition of intense ion bombardment consists of small concentration of hydrogen along with a mixture of sp^1 , sp^2 and sp^3 bonded carbon atoms [75,78]. The lattice energy of amorphous carbon (aC) is considerably smaller than in diamond, and can be placed between

diamond and graphite with more diamond-like properties associated with aC coatings having higher concentration of sp^3 bonded carbon and more graphite-like properties associated with aC coatings having lower concentration of sp^3 bonded carbon atoms [75,85]. This consideration allows formulation of an amorphous carbon model as a solid solution, including graphite and hypothetical amorphous carbon aC phase having higher lattice energy than that of graphitic carbon. Fig. 12d represents the results of thermodynamic calculations, where amorphous carbon matrix was modeling as a solid solution including β -Graphite (bC) and hypothetical amorphous carbon phase (aC) having enthalpy of formation ranging from 200 to 1000 J/mol K, while other parameters of this phase were taken the same as that of graphite. The results obtained in these calculations show that aC solubility in bC/aC modeling solution decreases from 50% to 40% when the enthalpy of formation of the aC phase increases from 200 to 1000 J/mol K. In addition, the results of calculations show that variation of the enthalpy of formation of aC carbon phase appears to have little influence on the solubility of carbon in B_4C/C , TiB_2/C and TiC/C solid solutions. Taking into account the lack of direct experimental data of amorphous carbon binding energies in TiBC coatings, the enthalpy of formation of aC atoms when modeling the C/aC solid solution was taken as $H_f(aC)=200$ J/mol K for further calculations. In this case, the free carbon constitutes near equal amount of graphite and amorphous carbon phase, which appears to be more realistic than the graphite/diamond solution model. The solubility of carbon in TiB_2 and B_4C at temperatures less than 1000 K does not exceed 15% and 25% respectively. These results are in good agreement with theoretical and experimental data [49–51,68,72–74,86].

The calculation results for the TiBC system with lower boron amount, using the same model, including 16 binary solutions in addition to the bC/aC solid solution (representing the free carbon phase), are presented in Fig. 12e. The difference between results presented in Fig. 12d and e is that TiC replaces B_4C when the boron concentration is low. The concentration of the TiC/C solid solution is nearly equal to the concentration of TiB_2/C solution. The carbon solubility in TiC does not exceed 18%, and slightly increases when carbon content increases. These results are also in good agreement with experimental data and theoretical calculations [68,72–74,86]. These results provide validity for the chosen set of solid solutions including free carbon modeling in the thermodynamic modeling calculations.

These models show that in all cases, a relatively high concentration of TiB_2 is present throughout all ranges of parameters representative of the FAD/UBM coating deposition process. TiB_2 co-exists either with B_4C (higher boron concentration) or with TiC (lower boron concentration), in agreement with ternary phase diagrams. More detailed calculations revealed that B_4C and TiC phases coexist (in low concentrations) in a relatively narrow Ti concentration window – in the transition zone between B_4C , as the sole carbide phase, and TiC as the sole carbide phase. These modeling results agree with those produced previously, including the phase diagram of nonstoichiometric Ti–B–C compounds [49–51,69,71]. It was shown that small B addition

(<1 at.%) creates disordering in TiC, resulting in the formation of titanium borides (TiB , TiB_2 , and Ti_3B_4). At high boron concentrations, TiB_2 coexists with B_4C and free carbon. At high Ti concentrations, titanium borides coexist with free carbon and TiC, which replaces B_4C in a titanium enriched TiBC composition. This occurs in a wide range of temperatures (500–1800 K), where the phase diagram has two well-defined areas: one with predominately TiB_2+TiC ; and another with predominately TiB_2+B_4C , and possible solid solutions [49–51]. The results of thermodynamic modeling assist in the interpretation of XRD patterns from the TiBC coatings in this study (Fig. 10). During the deposition, the substrates are exposed to Ti, C and B containing metal-gaseous vapor plasmas depending upon the position of substrates in the FAPSID system chamber (e.g. either near the LAFAD titanium plasma source, or UBM boron–carbon sputtering source). This provides continuous formation of the most stable (TiB_2) crystalline phase and smaller concentrations of complex Ti–B–C solid solutions, embedded within a quasi-amorphous matrix formed by Ti and B doped diamond-like carbon.

Increase of the elemental carbon concentration in the plasma environment due to increase of the flowrate of C–H gas concentration (methane or acetylene) results in the increase of free carbon and a decrease of carbide and boride based solid solutions of the TiBC coating segment since the carbon concentration in solid solution cannot exceed the solubility limit. These results are in good agreement with experimental data presented in Figs. 7 and 8, which provide evidence for the existence of free carbon in TiBC coatings deposited by hybrid FAD/UBM technique. Similar results were obtained for deposition of boron carbide coatings by magnetron sputtering with addition of methane, where the amount of boron in coatings was decreased and carbon concentration was increased with the increase of CH_4 gas flow [27,77].

Different phase compositions of the deposited TiBC top coating segment have different mechanical properties. Optimizing the concentration of the hard boride and carbide phases in the carbon matrix allows control of the coating hardness, as illustrated in Table 2. The maximum hardness was achieved with the increase of the concentration of C–H gas (8 sccm for methane or 4 sccm for acetylene) which can be explained by contribution of titanium based borides and carbides into the ternary Ti–B–C coating. The Resistance to Plastic Deformation Parameter (RPDP) H^3/E^{*2} also reaches a maximum value when the methane flowrate is at 8 sccm. It should be noted that greater values of the RPDP parameter do not always correlate with actual wear or fracture resistance performance of coatings. There are a number of ways of toughening coatings such as nanostructuring, grain size optimization, composition and structure grading as outlined in Ref. [82]. The free carbon content reduces coating stresses, allows control of coating toughness and reduces the negative effect of high brittleness inherent in coatings composed of the hard carbide and boride phases. This could explain the results of the Rockwell C indentation and scratch adhesion testing. Addition of free carbon can also contribute to lower friction and higher wear resistance of the top coating segment [14,27,77].

From Table 2, coatings deposited with single rotation exhibit higher hardness than those deposited with double rotation and having higher carbon concentration. It has to be noticed that coating structure and morphology are different between TiBC coatings prepared with single and double rotation, which can influence functional properties of the coatings such as adhesion and hardness. Coatings deposited with double rotation have greater roughness than coatings deposited with single rotation. In addition to differences in chemical composition, FAD/UBM TiBC coatings deposited with double rotation are subjected to a lower flux of energetic titanium ions generated by LAFAD plasma source in comparison to the coatings deposited with double rotation. This leads to reduction of adatom mobility at low deposition temperatures, resulting in favorable columnar growth according to Thornton–Messier zone diagram [11]. This observation is also in agreement with results obtained in [76].

5. Conclusions

Multilayer nanocomposite cermet coatings have been developed which consists of two segments: the bottom multilayer nanolaminated TiCr/TiCrN bondcoating corrosion resistant segment, interfacing the steel substrate followed by a top tribological TiBC segment. The metallic interlayers in the TiCr/TiCrN bottom segment contribute to the increase of corrosion resistant properties as well as improvement in coating adhesion and toughness. The TiBC nanocomposite top coating segment consists of titanium carbide and boride crystals embedded in a hard amorphous carbon matrix. Co-deposition of 100% ionized titanium filtered arc vapor plasma with sputtering B–C flow in a highly ionized argon–hydrocarbon gaseous plasma environment allows precise control of the coating elemental composition, which correlates with its mechanical properties. Experimental evaluation and thermodynamic modeling suggest the structure of the top TiBC coating segment includes strongly crystallized non-stoichiometric TiB₂ with weakly crystallized ternary and binary solid solutions and non-stoichiometric carbide phases of the TiBC elemental system incorporates into an amorphous carbon matrix. This coating deposited by hybrid FAD/UBM technology has demonstrated extremely high toughness and adhesion at hardness levels comparable to conventional hard cermet coatings, which make the coating and a deposition method a promising candidate for tribological tasks in high load aircraft applications.

References

- [1] Alloy Data, Carpenter Technology Corporation via www.carpenter.com.
- [2] J.A. Jehn, Surf. Coat. Technol. 125 (2000) 212.
- [3] M.J. Park, A. Leyland, A. Matthews, Surf. Coat. Technol. 43/44 (1990) 481.
- [4] M. Hans, E. Bergmann, Surf. Coat. Technol. 62 (1993) 626.
- [5] P.K. Vencovsky, R. Sanchez, J.R.T. Branco, M. Galvano, Surf. Coat. Technol. 108–109 (1998) 599.
- [6] Vladimir Gorokhovskiy, Brad Heckerman, Philip Watson, Nicholas Bekesch, Surf. Coat. Technol. 200 (18–19) (2006) 5614.
- [7] H.W. Wang, M.M. Stack, S.B. Lyon, P. Hovsepian, W.-D. Munz, Surf. Coat. Technol. 126 (2000) 279.
- [8] O. Knotek, F. Löffler, A. Schrey, B. Bosserhoff, Surf. Coat. Technol. 126 (2000) 138.
- [9] Z. Has, S. Mitura, V. Gorokhovskiy, Surf. Coat. Technol. 47 (1991) 106.
- [10] N. Novikov, V.I. Gorokhovskiy, B. Uryukov, Surf. Coat. Technol. 47 (770) (1991).
- [11] R.L. Boxman, D.M. Sanders, P.J. Martin, Handbook of Vacuum Arc Science and Technology, Noyes Publications, Park Ridge, N.J., 1995.
- [12] D. Sanders, A. Anders, Surf. Coat. Technol. 139 (2000).
- [13] Hermann A. Jehn, Surf. Coat. Technol. 131 (2000) 433.
- [14] K. Bewilogua, C.V. Cooper, C. Specht, J. Schroder, R. Wittorf, M. Grischke, Surf. Coat. Technol. 132 (2000) 275.
- [15] Y.L. Su, W.H. Kao, Surf. Coat. Technol. 137 (2001) 293.
- [16] M.P. Delpancke-Ogletree, O.R. Monteiro, Surf. Coat. Technol. 108–109 (1998) 484.
- [17] E. Bertran, C. Corbella, A. Pinyol, M. Vives, J.L. Andujar, Diamond Relat. Mater. 12 (2003) 1008.
- [18] M. Jarratt, J. Stallard, N.M. Renevier, D.G. Teer, Diamond Relat. Mater. 12 (2003) 1003.
- [19] A. Erdemir, C. Bindal, G.R. Fenske, C. Zuiker, P. Wilbur, Diamond Relat. Mater. 86–87 (1996) 692.
- [20] A. Erdemir, O.L. Eryilmaz, I.B. Nilufer, G.R. Fenske, Surf. Coat. Technol. 133–134 (2000) 448.
- [21] D. Paulmier, H. Zaidi, H. Nery, T.L. Huu, T. Mathia, Surf. Coat. Technol. 62 (1993) 570.
- [22] B. Podgornik, S. Jacobson, S. Hogmark, Proceedings of World Tribology Congress I, Vienna, 2001, p. 843.
- [23] J.S. Zabinsky, J.H. Sanders, J. Najnaparamph, *ibid.*,
- [24] A.A. Voevodin, J.P. O'Neill, J.S. Zabinski, Surf. Coat. Technol. 116–119 (1999) 36.
- [25] A.A. Voevodin, J.S. Zabinski, Diamond Relat. Mater. 7 (1998) 463.
- [26] Frederik Svahn, Tribology of Carbon Based Coatings for Machine Element Applications Acta Universitatis Upsaliensis. Comprehensive Summaries of Uppsala Dissertations from the Faculty of Science and Technology 1050. 40 pp. Uppsala, 2004.
- [27] T. Eckardt, K. Bewilogua, G. van der Kolk, T. Hurkmans, T. Trinh, W. Fleischer, Surf. Coat. Technol. 126 (2000) 69.
- [28] A.A. Voevodin, M.A. Capano, A.J. Safriet, M.S. Donley, J.S. Zabinski, Appl. Phys. Lett. 69 (188) (1996).
- [29] P.S. Kisliy (Ed.), Cermet, Monograph, Institute of Superhard Materials of the Ukrainian Academy of Sciences, Kiev, 1985.
- [30] E.H.A. Dekempeneer, V. Wagner, L.J. van IJzendoorn, J. Meneve, S. Kuypers, J. Smeets, J. Geurts, R. Caudano, Surf. Coat. Technol. 86–87 (1996) 581.
- [31] S.J. Harris, G.G. Krauss, S.J. Simko, R.J. Baird, S.A. Gebremariam, G. Doll, Wear 252 (2002) 161.
- [32] Vladimir I. Gorokhovskiy, Rabi Bhattacharya, Deepak G. Bhat, Surf. Coat. Technol. 140 (2) (2001) 82.
- [33] V.I. Gorokhovskiy, D.G. Bhat, R. Bhattacharya, A.K. Rai, K. Kulkarni, R. Shivpuri, Surf. Coat. Technol. 140 (3) (2001) 215.
- [34] V. Gorokhovskiy, US Patent No.6,663,755.
- [35] D. Nilsson, F. Svahn, U. Wiklund, S. Hogmark, Wear 254 (2003) 1084.
- [36] W.-D. Munz, T. Hurkmans, G. Keiren, T. Trinh, J. Vac. Sci. Technol., A, Vac. Surf. Films 11 (5) (Sep/Oct 1993) 2583.
- [37] J. Valli, U. Makela, A. Matthews, Surf. Eng. 2 (1986) 49.
- [38] G.G. Stoney, Proc. R. Soc. Lond., A 82 (1909) 172.
- [39] W.C. Oliver, G.M. Pharr, J. Mater. Res. 7 (1992) 1564.
- [40] M. Chiari, et al., Nucl. Instrum. Methods Phys. Res., B Beam Interact. Mater. Atoms 184 (2001) 309.
- [41] M. Mayer, SIMNRA User's Guide, Technical Report IPP 9/113, Max-Planck-Institute für Plasmaphysik, Garching, Germany, 1997.
- [42] M. Bielewski, R. Holt, A Review of Sacrificial Coatings to Replace Cadmium, Report No.LTR-ST-2174, Institute for Aerospace Research, NRC Canada.
- [43] S.J. Bull, D.G. Bhat, M.H. Staia, Surf. Coat. Technol. 163–164 (2003) 499.
- [44] J.R. Tuck, A.M. Korsunsky, D.G. Bhat, S.J. Bull, Surf. Coat. Technol. 139 (2001) 63.
- [45] C.A. Davis, Thin Solid Films 226 (1993) 30.
- [46] N.A. Vatolin, G.K. Moiseev, B.G. Trusov, Thermodynamic Modeling in High Temperature Inorganic Systems, Metallurgy, Moscow, 1994 (in Russian).

- [47] L.V. Gurchich, I.V. Veitz, et al., Thermodynamic Properties of Individual Substances. Forth edition in 5 Volumes, vol. 1, Hemisphere Pub., Co., New York, 1989, in 2 parts.
- [48] NIST-JANAF, in: M.W. Chase Jr. (Ed.), Thermochemical Tables, Fourth edition, J. of Physical and Chemical Reference Data, Monograph, vol. 9, 1998.
- [49] A.I. Gusev, A.A. Rempel, A. Magerl, Disorder and Order in Strongly Non-Stoichiometric Compounds, Springer, 2001, p.607.
- [50] H. Duschaneck, P. Rogl, H.L. Lukas, J. Phase Equilibria 16 (1995) 46.
- [51] P. Rogl, H. Bittermann, International Journal of Refractory Metals and Hard Materials 17 (1999) 32.
- [52] A.A. Voevodin, S.D. Walck, J.S. Zabinski, Wear 203–204 (1997) 516.
- [53] A.A. Voevodin, J.S. Zabinski, J. Mater. Sci. 33 (1998) 319.
- [54] A.A. Voevodin, J.P. O'Neill, J.S. Zabinski, Surf. Coat. Technol. 116–119 (1999) 36.
- [55] A.A. Voevodin, J.S. Zabinski, Thin Solid Films 370 (2000) 223.
- [56] A.A. Voevodin, M.A. Capano, S.J.P. Laube, M.S. Donley, J.S. Zabinski, Thin Solid Films 298 (1997) 107.
- [57] A.A. Voevodin, J.S. Zabinski, Compos. Sci. Technol. 65 (2005) 741.
- [58] K. Miyoshi, B. Pohlchuck, K.W. Street, J.S. Zabinski, J.H. Sanders, A.A. Voevodin, R.L.C. Wu, Wear 225–229 (1999) 65.
- [59] A.A. Voevodin, J.P. O'Neill, J.S. Zabinski, Thin Solid Films 342 (1999) 194.
- [60] In-Wook Park, Kwang Ho Kim, A.O. Kunrath, D. Zhong, J.J. Moore, A.A. Voevodin, E.A. Levashov, J. Vac. Sci. Technol., B 23 (2005) 588.
- [61] A.A. Voevodin, J.S. Zabinski, in: A.A. Voevodin, D.V. Shtansky, E.A. Levashov, J.J. Moore (Eds.), Nanostructured thin films and nanodispersion strengthened coatings, Kluwer Academic Publishers, Dordrecht, The Netherlands, 2004, p. 103.
- [62] A.A. Voevodin, M.A. Capano, A.J. Safriet, M.S. Donley, J.S. Zabinski, Appl. Phys. Lett. 69 (1996) 188.
- [63] A.A. Voevodin, J.G. Jones, T.C. Back, J.S. Zabinski, V.S. Strel'nitzki, I.I. Aksenov, Surf. Coat. Technol. 197 (2005) 116.
- [64] D.E. Wert, et al., US Patent 5002729.
- [65] James L. Maloney, Adv. Mater. Process. 7 (1) (1998).
- [66] Hitesh K. Trivedi, Costandy S. Saba, Lisa C. Carswell, Lois J. Gschwendler, Carl E. Snyder, Tribol. Lett. 5 (1998) 211.
- [67] R.J. Smith, C. Tripp, A. Knospe, C.V. Ramana, A. Kayani, Vladimir Gorokhovskiy, V. Shutthanandan, D.S. Gelles, J. Mater. Eng. Perform. 13 (2003) 295.
- [68] P.E. Gannon, C.T. Tripp, A.K. Knospe, C.V.R. Ramana, M. Deibert, R.J. Smith, V.I. Gorokhovskiy, V. Shutthanandan, D. Gelles, Surf. Coat. Technol. 188–189 (2004) 55.
- [69] P.J. Spencer, H. Holleck, High Temp. Sci. 27 (1990) 295.
- [70] A.C. Victor, J. Am. ceram. Soc. 36 (7) (1962) 1903.
- [71] V. Linss, S.E. Rodil, P. Reinke, M.G. Garnier, P. Oelhafen, U. Kreissig, F. Richter, Thin Solid Films 467 (2004) 76.
- [72] V.I. Malkovich (Ed.), Boron and Refractory Borides, Springer, Verlag, 1977.
- [73] G.V. Samsonov, T.I. Serebryakova, V.A. Neronov, Borides, Atmoisdat, Moscow, 1975, p374 (In Russian).
- [74] P.S. Kisliy, M.A. Kusenkova, N.I. Bodnaruk, B.L. Grabchuk, Boron Carbide, Naukova Dumka, Kiev, 1988 (in Russian).
- [75] J. Robertson, Pure and Appl. Chem., Vol. 66, No. 9, pp. 1789–1796.
- [76] N. Panich, Y. Sun, Thin Solid Films 500 (2006) 190.
- [77] H.-S. Ahn, P.D. Cuong, K.-H. Shin, Ki-Seung Lee, Wear 259 (2005) 807.
- [78] D.R. McKenzie, J. Vac. Sci. Technol., B 11 (1993) 1928.
- [79] H. Liepak, K. Bartsch, B. Arnold, H.-D. Bauer, X. Liu, M. Knupfer, A. Leonhardt, Diamond Relat. Mater. 13 (2004) 106.
- [80] E. Amberger, H.P. Gerster, Acta Crystallogr., B 36 (1980) 672.
- [81] D.D. Wagman, et al., J. Phys. Chem. Ref. Data 11 (supp. 2) (1982).
- [82] Sam Zhang, Deen Sun, Yougqing Fu, Hejun Du, Surf. Coat. Technol. 198 (2005) 2.
- [83] J. Musil, F. Kum, H. Zeman, H. Polakova, Surf. Coat. Technol. 154 (304) (2002).
- [84] M. Stoiber, S. Perlot, C. Mitterer, M. Beschliesser, C. Lugmair, R. Kullmer, Surf. Coat. Technol. 177 (348) (2004).
- [85] A. Lysenko, V. Gorokhovskiy, Y. Nikitin, V. Poltoratsky, Molecular Model of Diamond-like Carbon Structure Synthesized under Low Pressure, Reports of the Academy of Sciences of the UkrSSR, 1989 (in Russian).
- [86] Handbook of Refractory Carbides and Nitrides, By: Pierson, H.O., William Andrew Publishing/Noyes, 1996.